World Academy of Science, Engineering and Technology
International Journal of Electronics and Communication Engineering
Vol:16, No:11, 2022

Combining an Optimized Closed Principal Curve-Based Method and Evolutionary Neural Network for Ultrasound Prostate Segmentation

Tao Peng, Jing Zhao, Yanqing Xu, Jing Cai

***Abstract*—**Due to missing/ambiguous boundaries between the prostate and neighboring structures, the presence of shadow artifacts, as well as the large variability in prostate shapes, ultrasound prostate segmentation is challenging. To handle these issues, this paper develops a hybrid method for ultrasound prostate segmentation by combining an optimized closed principal curve-based method and the evolutionary neural network; the former can fit curves with great curvature and generate a contour composed of line segments connected by sorted vertices, and the latter is used to express an appropriate map function (represented by parameters of evolutionary neural network) for generating the smooth prostate contour to match the ground truth contour. Both qualitative and quantitative experimental results showed that our proposed method obtains accurate and robust performances.

***Keywords*—**Ultrasound prostate segmentation, optimized closed polygonal segment method, evolutionary neural network, smooth mathematical model.

I. Introduction

DIAGNOSING and treating prostate cancer continues to burden global populations as it is one of the most common noncutaneous cancers and the second leading cause of cancer-related deaths in men [1]. Accurate segmentation of the prostate plays an important role in biopsy needle placement, radiotherapy treatment planning, and motion monitoring [2]. However, it is still a challenging task due to the following reasons: (1) missing boundary caused by the artifacts and the presence of other surrounding structures (i.e., the bladder and seminal vesicles), (2) ambiguous boundary due to low soft-tissue contrast in transrectal ultrasound (TRUS) images, (3) inhomogeneous intensity distribution of the prostate tissue, and (4) various shape of the prostate between different patients.

The current prostate segmentation techniques can be briefly summarized into two groups, fully-automatic methods and semi-automatic methods.

Fully-automatic methods: Automatic prostate segmentation in TRUS images has become a hot research area in recent years [3], [4]. Orlando et al. [4] used the modified U-Net for automatic prostate segmentation on clinically diverse three-dimensional (3D) TRUS images. The proposed method contains two steps: (1) two-dimensional (2D) prediction step based on 2D modified U-Net (mU-Net) to achieve a 2D prostate surface; (2) 3D reconstruction step to connect all the 2D connected boundaries so to a generate 3D prostate surface. The proposed method demonstrated overall segmentation results for 2D Dice Similarity Coefficient (DSC), 3D DSC of 94.9% and 94.1%, respectively. The limitation of the study is the use of only one observer for providing ground truth segmentations, which means it could not directly assess interobserver variability for the dataset. In addition, the authors have not directly assessed intra-observer variability over several time points. Ghavami et al. [5] proposed an automatic slice segmentation method in intraoperative TRUS images using convolutional neural networks. Furthermore, based on their previous work [5], Ghavami et al. [6] further proposed an improved convolutional neural network for ultrasound prostate segmentation by adding two improvements, such as 1) incorporating neighboring slices into the network to use 3D information for each slice, and 2) using additive up-sampling shortcut architecture to accelerate training time and improve performance. The DSC of the method was 89%. However, the ground truth of both works was obtained by only one physician, which may more likely generate delineation errors without other physicians' checks.

Semi-automatic methods: In semi-automatic prostate segmentation methods, the involvement of a radiologist or an expert is often used to initialize the segmentation process or sometimes to correct the final segmentation result [7]. To minimize human involvement, many research works have been reported for semi-automatic prostate segmentation [8]. Zeng et al. [9] proposed a convolutional neural network to segment the prostate in TRUS images alternative and uses magnetic resonance imaging (MRI) priors with good performance. However, the authors have not characterized the segmentation error by computing a target registration error using more tissue landmarks, such as the segmented urethra, bladder, or rectum wall. Karimi et al. [10] developed a two-step method for accurate segmentation of the prostate clinical target volume in TRUS images. The first step was to use an adaptive sampling strategy to assist CNN to pay more attention to some images that are difficult to segment before the training process. The

Tao Peng is with the School of Future Science and Engineering, Soochow University, Suzhou, China (e-mail: sdpengtao401@gmail.com).

Jing Zhao is with the Department of Ultrasound, Tsinghua University Affiliated Beijing Tsinghua Changgung Hospital, Beijing, China (e-mail: zja01281@btch.edu.cn).

Yanqing Xu is with the McDermott Center for Human Growth and Development, University of Texas Southwestern Medical Center, Dallas, Texas, USA (e-mail: yanqing.xu@utsouthwestern.edu).

Jing Cai was with Duke University, Durham, North Carolina, USA. He is now with the Department of Health Technology and Informatics, The Hong Kong Polytechnic University, Hong Kong, China (corresponding author, e-mail: jing.cai@polyu.edu.hk).

second step is to identify the uncertain segmentations during training, whilst using the prior shape information in the form of a statistical shape model to improve the accuracy of uncertain segmentations. The DSC of the method is 93.9 ± 3.5%. However, all images of this study were collected using ultrasound machines and probe from a single manufacturer, where the universality of the proposed method was not tested. Furthermore, the ground truths provided by expert radiation oncologists on TRUS images can be biased at the prostate base and apex.

Recent TRUS image segmentation works include automatic and semi-automatic methods. The DSC of most automatic models [3], [4] is only near 0.9. In this work, we propose a semi-automatic segmentation model with radiologist-defined seed points as the prior and aim to obtain high accuracy results.

Our main contributions are summarized as follows: (1) it takes advantage of the principal curve's characteristic to approximate the dataset's center automatically and uses the learning ability of the neural network to decrease model error; (2) to avoid generating a distorted principal curve by the influence of abnormal data points, based on our previously proposed closed principal curve method, we designed an optimized closed polygonal segment method (OCPS) by newly adding a vertex cleaning and optimization step; (3) to find the optimal Caputo fractional-order backpropagation training network (CFBT), we propose the dynamic storage-based differential evolution method (DSDE) by combining the historical storage-based and dynamic population size mechanism, whilst innovatively using multi-mutation operators to guarantee the population diversity and newly added constraint conditions to acquire the optimal parameters of the differential evolution-based model; and, (4) we design an appropriate map function (represented by parameters of evolutionary neural network) for generating the smooth prostate contour to match the ground truth contour.

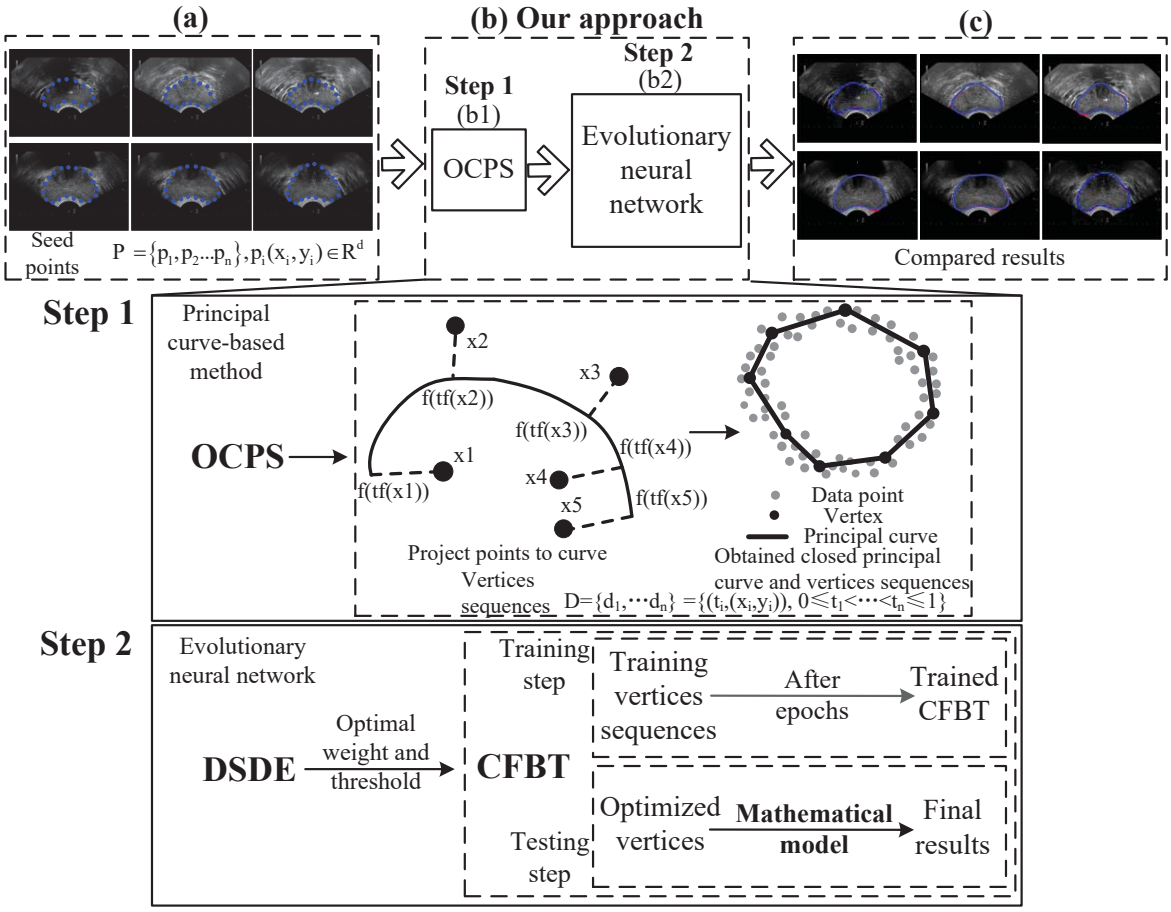

Fig. 1 Overall architecture of the proposed method

II. Our Approach

A. Overall

For accurate prostate contour detection, our method mainly contains two steps: (1) the first step is to use the OCPS to generate a closed contour consisting of line segments connected by sorted vertices by using a small number of radiologist-defined seed points as point-based prior (Section II *B*), (2) the second stage is to find a suitable map function (realized by the evolutionary neural network) to generate a smooth prostate contour denoted by the output of neural network (i.e., optimized vertices) to match the ground truth contours (Section II *C*). The flowchart of the proposed method is shown in Fig. 1.

B. OCPS

1) Finding Principal Curve

Principal curve was first defined as a smooth one-dimensional curve that passes through the middle of an *n*-dimensional data set, providing a nonlinear summary of the data [11]. Based on the definition of principal curve, Kegl et al. proposed the Polygonal Line (PL) method for finding the *k*-segment principal curve [12], [13]. The key steps of the PL method are projection and vertex optimization steps. The projection step is mainly used to classify the data points based on which vertex or edge they project. Meanwhile, the vertex optimization step is used to update the position of each vertex and line segment based on the principle of the nearest distance from the data points to the principal curve [12]. Fig. 2 shows the details of finding the principal curve. From Fig. 2 (a), the first principal component line is used as a starting curve, which consists of vertex v_1 and v_2. By inserting a new vertex v_2, all the vertices are updated such that the principal curve is updated, shown in Fig. 2 (b). Fig. 2 (c) shows that the old vertex is replaced and a new vertex is added, which is according to the principle of nearest distance from the point to principal curve [12]. Principal curve is updated along with the added new vertex (Fig. 2 (d)), and a contour consisting of line segments is generated (Fig. 2 (e)).

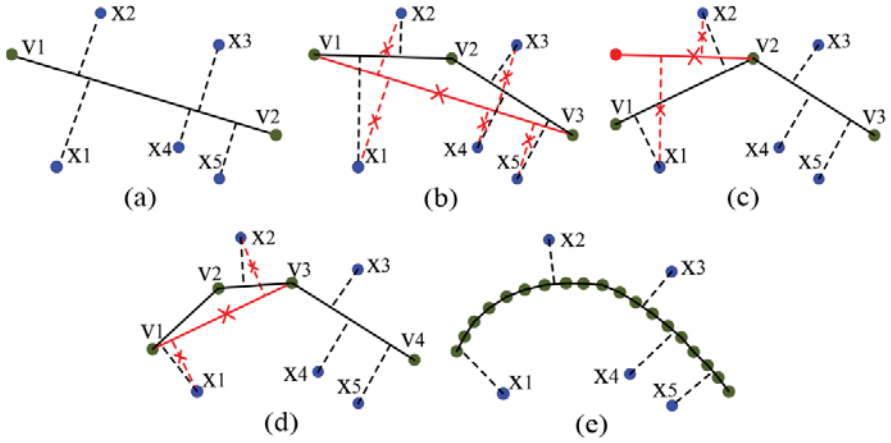

Fig. 2 Finding principal curve. x denotes the initial points: v denotes the vertex, black line shows the principal curve, red line shows the deleted curve, and black dashed line shows that the data point is projected to the principal curve

2) Closed Polygonal Segment Method

Based on the PL method [13], we have previously proposed a semi-automatic method [14] named Closed Polygonal Segment (CPS) that added several improvements (i.e., initialization, normalization, stop conditions, and constraint conditions) for medical image segmentation.

3) OCPS

Compared with our previous work (CPS), the OCPS mainly added two improvements: (1) we use an improved vertex optimization step [15]; and (2) we add a vertices cleaning method for cleaning the abnormal vertices, shown as follows: Firstly, we initialize the vertex cleaning label flag(v_i) with 1; then when the length l_{si} of i-th line segment is more than or equal to data radius r, we set flag(v_i) as 1 and reserve the vertex v_i; otherwise, we remove the vertex v_i. r as data radius is used to determine the data scaling and should meet the condition below:

$$r = \max \left\| x - \frac{1}{n} \sum_{y \in P} y \right\| \quad (1)$$

where P is the data points set, and n is the number of data points, x and y are the x-axis and y-axis coordinates of the data point pi, respectively.

C. Evolutionary Neural Network

The classical neural network (NN) with gradient-based optimization suffers from the drawback, such as the tendency of being trapped in the local optimum. In this work, we use the DSDE method to search global optimal parameters (i.e., connection weights and thresholds) for the CFBT network. Then find an appropriate map function (achieved by three-layer CFBT) to make the prostate contour smooth, where the smooth prostate contour is denoted by the output of the NN (i.e., optimized vertices) to match the ground truth contours.

Compared with Leema et al. [16], we proposed the DSDE by adding several improvements, including 1) historical storage-based mechanism [17], 2) dynamic population size [18], 3) multi-mutation operators, and 4) constraint conditions. The key steps of DSDE are as follows:

i. initialize the mean mutation Factor (uF) and mean Crossover Rate (uCR) within the range of [0, 1].
ii. set the current iteration number G = 1 and define G < the max iteration number G_{max}.
iii. if G is larger or equal to G_{max}, turn to step (x); or G = G+1, then turns to step (ii)
iv. in the mutation step, the new mutant individual v_i^{G+1} is generated using *multi-mutation operators*, shown as:

$$v_i^{G+1} = \begin{cases} x_{i1}^G + \text{rand}_1 \times (x_{i2}^G - x_{i3}^G), \text{if rand}[0,1] < P_G \\ x_{i1}^G + \text{rand}_2 \times (x_{i2}^G - x_{i3}^G) + \text{rand}_3 \times (x_{i4}^G - x_{i5}^G), \text{otherwise} \end{cases} \quad (2)$$

v. in crossover step, the experimental individual u_i^{G+1} is achieved based on [19], shown as:

$$u_i^{G+1} = \begin{cases} v_i^{G+1}, \text{if rand}[0,1] < CR \\ x_i^G, \text{otherwise} \end{cases} \quad (3)$$

vi. during the selection step, the next candidate x_i^{G+1} is achieved based on [19], shown as:

$$x_i^{G+1} = \begin{cases} u_i^{G+1}, \text{if } f(u_i^{G+1}) < f(x_i^G) \\ x_i^G, \text{otherwise} \end{cases} \quad (4)$$

vii. the new population size n is obtained using the *dynamic population size* principle [18].

viii. through the added *constraint conditions*, the next individual x_i^{G+1}, successful probability S(uF), and S(uCR) are updated. The *constraint conditions* are shown as: 1) If $f(v_i^G)$ is less than or equal to $f(x_i^G)$, we set v_i^G equal to the next individual x_i^{G+1}, and 2) If $f(v_i^G)$ does not equal $f(x_i^G)$, we set p_G to S(uF) or S(uCR); otherwise, we set the previous individual x_i^G to the next individual x_i^{G+1}.

ix. both uF and uCR are updated based on the *historical storage-based mechanism* [17]. When G < GMax, we set G = G+1, and then it turns to step (ii), where the newly obtained uF and uCR will be used for the next loop. Otherwise, if G ≥ GMax, it turns to step (x).

x. the best individual can be selected.

After determining the initial parameters (i.e., connection weights and thresholds) of the CFBT by the DSDE, we will train the three-layer CFBT. Due to obtaining vertices consisting of x and y-axis coordinates, the output layer of the CFBT contains two units, corresponding to x and y, where x and y can be treated as the continuous functions c(x(t)) and c(y(t)), respectively, on the sequence number of vertices t [14]. Two output neurons c(•) of the output layer of the CFBT are described as:

$$(c(x(t), c(y(t))) = \left(\frac{e^{\sum_{i=1}^{Z}\frac{1}{1+e^{-(t\omega_i - T_i)}}v_{i,1}-b_1} - e^{-\left(\sum_{i=1}^{Z}\frac{1}{1+e^{-(t\omega_i - T_i)}}v_{i,1}-b_1\right)}}{e^{\sum_{i=1}^{Z}\frac{1}{1+e^{-(t\omega_i - T_i)}}v_{i,1}-b_1} + e^{-\left(\sum_{i=1}^{Z}\frac{1}{1+e^{-(t\omega_i - T_i)}}v_{i,1}-b_1\right)}}, \frac{e^{\sum_{i=1}^{Z}\frac{1}{1+e^{-(t\omega_i - T_i)}}v_{i,2}-b_2} - e^{-\left(\sum_{i=1}^{Z}\frac{1}{1+e^{-(t\omega_i - T_i)}}v_{i,2}-b_2\right)}}{e^{\sum_{i=1}^{Z}\frac{1}{1+e^{-(t\omega_i - T_i)}}v_{i,2}-b_2} + e^{-\left(\sum_{i=1}^{Z}\frac{1}{1+e^{-(t\omega_i - T_i)}}v_{i,2}-b_2\right)}}\right) \quad (5)$$

where t is the sequence number of vertices, and Z is the number of hidden neurons. w_i(i = 1,2,…,Z) and $v_{i,u}$(i = 1,2,…,Z; u = 1,2) are the weights from the input layer to the i-th hidden neuron and from the i-th hidden neuron to the u-th output neuron, respectively. b_u(u = 1,2) and T_i(i = 1,2,…,Z) are the thresholds of the u-th output and the i-th hidden neurons, respectively [20].

After the training, we will obtain the coordinates of optimized vertices to express smooth prostate contour, shown as:

$$f(t) = \big(x(t), y(t)\big) = \left(\frac{c(x(t) + 1 - \sqrt{1 - \big(c(x(t))\big)^2}}{2 \times c(x(t))}, \frac{c(y(t)+1-\sqrt{1-\big(c(y(t))\big)^2}}{2\times c(y(t))}\right) \quad (6)$$

where x(t) and y(t) denote the x-axis and y-axis coordinate of the contour points, respectively.

D. Materials

A dataset consisting of 300 brachytherapy patients is used to prove the performance of our approach, where the dataset was independently collected from the Tsinghua University Affiliated Beijing Tsinghua Changgung Hospital. All TRUS data were collected on a Hitachi HI VISION Avius® ultrasound system and an integrated ultrasound high-resolution linear transducer with a frequency at the range of 4-8 MHz. The mechanical index was set to be 0.4, with a probe detection depth of 60 mm, a probe detection frequency of 9 MHz, and an amplifier gain between 15 and 40 dB. The original resolution of each TRUS image is 1024×768 pixels, and we have rescaled to 600×450 pixels. The ground truths are marked and determined by five board-certified radiologists. We randomly selected 200 patients for training, 60 patients for validation, and the remaining 40 patients for testing. All experiments are done on a computer with Intel Core i7-8750H CPU and Geforce GTX 1070 GPU with 8G memory.

III. Results

To prove the robustness of our approach, we have added different levels of Gaussian noise to corrupt the raw testing image, then tested on the corrupted testing images. Table I denotes the average testing results on different levels of Gaussian noise, where we select the Gaussian noise's standard deviation α in the range of [0, 100]. From Table I, the DSC, Ω, and Accuracy (ACC) of the proposed method are as high as 91.8%, 90.9%, and 91.4%, respectively, at the influence of Gaussian noise (standard deviation of Gaussian function σ = 100). Although σ changes from 0 to 100, the DSC, Ω, and ACC fluctuate around 5.18% at most, showing the excellent robustness of our method. Meanwhile, we randomly selected one slice with its corresponding results for visualization, shown in Fig. 3. In Fig. 3, the first row denotes the raw image (σ = 0) and other different levels of Gaussian noise (i.e., σ = 50 and 100) images. The second row is the corresponding histogram of the first-row images, where red and green regions denote the number of pixels at different gray values of raw and noise images, respectively. The third row denotes the compared results, where the red line shows the ground truth and the blue line shows the experimental results.

TABLE I
Results on Different Levels of Gaussian Noise

	DSC (%)	Ω (%)	ACC (%)
Raw set (σ = 0)	96.8	95.7	96.4
σ = 50	94	92.9	93.9
σ = 100	91.8	90.9	91.4

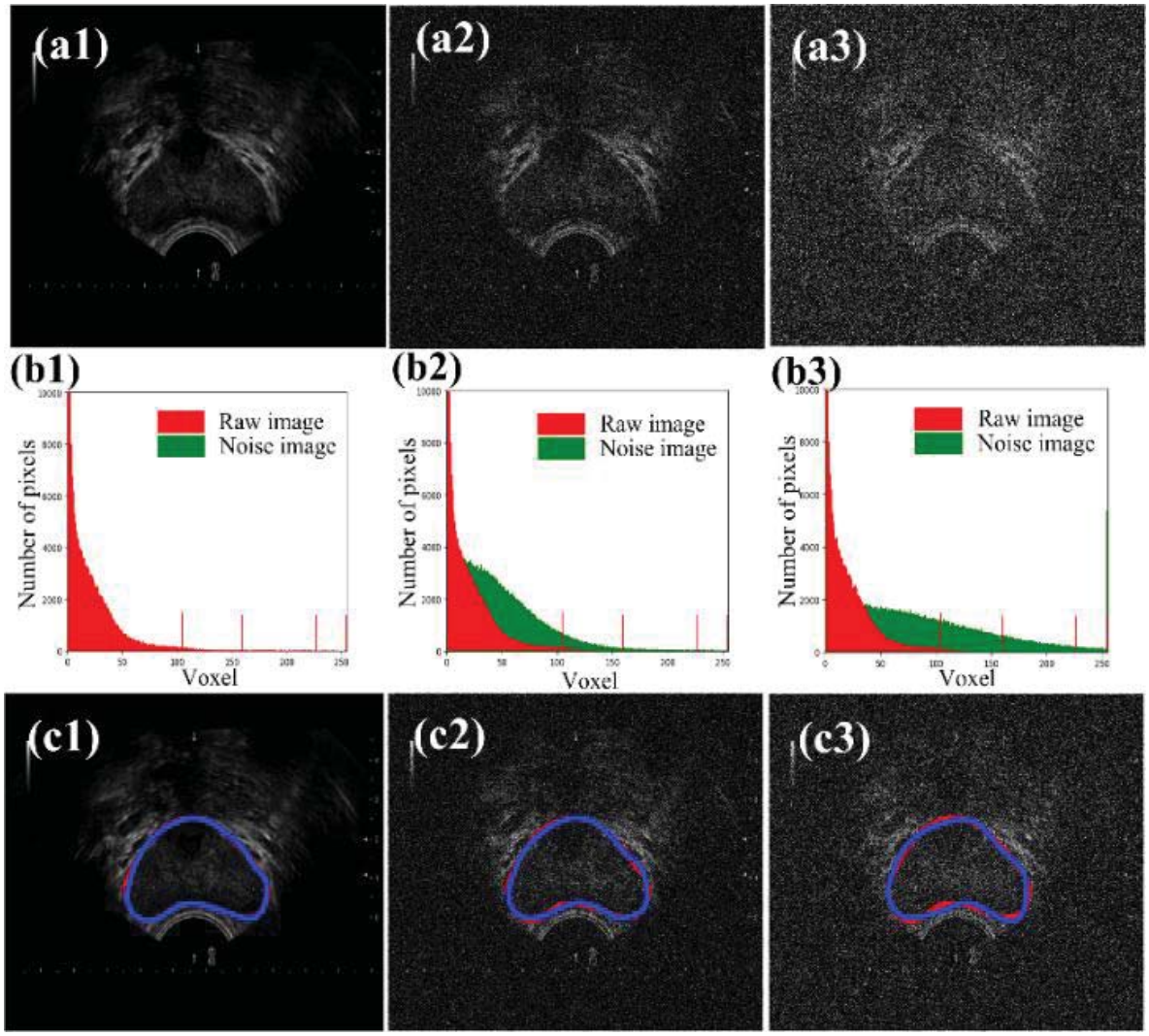

Fig. 3 Comparison on different levels of Gaussian noise

TABLE II
QUANTITATIVE COMPARISON WITH OTHER STATE-OF-THE-ART ALGORITHMS

Reference	Method	Model	DSC (%)	Ω (%)	ACC (%)
[21]	Mask-RCNN	Deep learning	91.6	90.2	91.3
[22]	Unet++	Deep learning	92.6	91.2	92.1
[23]	Hull-CPS	Hybrid	95.2	94.3	95.3
[24]	DBN-CPS	Hybrid	95.8	94.5	95.6
Proposed method	Our method	Hybrid	96.8	95.7	96.4

To further demonstrate the performance of our method, we use two kinds of state-of-the-art methods for comparison, including deep learning methods (Mask-RCNN [21] and Unet++ [22]), and hybrid methods (Hull-CPS [23] and Deep Belief Network (DBN)-CPS [24]).

All the hybrid methods integrate the principal curve-based model with machine learning. Two deep learning methods are fully-automatic and three hybrid methods are semi-automatic. Table II shows the quantitative segmentation results of all the methods. From Table II, all metrics of the hybrid methods are higher than the deep learning methods. The DSC, Ω, and ACC of the hybrid methods are at least 2.8%, 3.39%, and 3.47% higher than those of deep learning methods, respectively, which shows that the hybrid methods inherit the characteristics of data fitting of principal curve-based method so that the results of hybrid methods can better match the ground truth contour. Overall, our proposed method has the best performance.

IV. CONCLUSION

In this work, a hybrid approach is presented for accurate prostate segmentation in TRUS images. The DSC of most reported automatic methods [3] is only near 0.9. The goal of our work is to obtain accurate results using a small number of radiologist-defined seed points as point-based prior. To obtain accurate segmentation results, we combined an improved OCPS method and improved optimal parameters selection machine learning method. Furthermore, an appropriate map function (realized by three-layer machine learning) is found to make the prostate contour smooth. Results demonstrated that our method has good robustness and the better accuracy against state-of-the-art methods. Future work can be focused on the evaluation of different modalities or organs.

REFERENCES

[1] U. Swami, T. R. McFarland, R. Nussenzveig, and N. Agarwal, "Advanced Prostate Cancer: Treatment Advances and Future Directions," *Trends. in Cancer*, vol. 6, no. 8, pp. 702–715, 2020.

[2] Y. Lei *et al.*, "Ultrasound prostate segmentation based on multidirectional deeply supervised V-Net," *Med. Phys.*, vol. 46, no. 7, pp. 3194–3206, 2019.

[3] Y. Wang *et al.*, "Deep Attentive Features for Prostate Segmentation in 3D Transrectal Ultrasound," *IEEE Trans. Med. Imaging*, vol. 38, no. 12, pp. 2768–2778, 2019.

[4] N. Orlando, D. J. Gillies, I. Gyacskov, C. Romagnoli, D. D'Souza, and A. Fenster, "Automatic prostate segmentation using deep learning on clinically diverse 3D transrectal ultrasound images," *Med. Phys.*, vol. 47, no. 6, pp. 2413–2426, 2020.

[5] N. Ghavami *et al.*, "Automatic slice segmentation of intraoperative transrectal ultrasound images using convolutional neural networks," in *Medical Imaging 2018: Image-Guided Procedures, Robotic Interventions, and Modeling*, Houston, United States, 2018, p. 2.

[6] N. Ghavami *et al.*, "Integration of spatial information in convolutional neural networks for automatic segmentation of intraoperative transrectal ultrasound images," *J. Med. Imaging*, vol. 6, no. 1, 2018.

[7] R. P. Singh, S. Gupta, and U. R. Acharya, "Segmentation of prostate contours for automated diagnosis using ultrasound images: A survey," *J. Comput. Sci.*, vol. 21, pp. 223–231, 2017.

[8] S. Ghose *et al.*, "A supervised learning framework of statistical shape and probability priors for automatic prostate segmentation in ultrasound images," *Med. Image Anal.*, vol. 17, no. 6, pp. 587–600, 2013.

[9] Q. Zeng *et al.*, "Prostate segmentation in transrectal ultrasound using magnetic resonance imaging priors," *Int. J. Comput. Assist Radiol. Surg.*, vol. 13, no. 6, pp. 749–757, 2018.

[10] D. Karimi *et al.*, "Accurate and robust deep learning-based segmentation of the prostate clinical target volume in ultrasound images," *Med. Image Anal.*, vol. 57, pp. 186–196, 2019.

[11] T. Hastie and W. Stuetzle, "Principal Curves," *J. Am. Stat. Assoc.*, vol. 84, no. 406, pp. 502–516, 1989.

[12] B. Kegl and A. Krzyzak, "Piecewise Linear Skeletonization Using Principal Curves," *IEEE Trans. Pattern Anal. Mach. Intell.*, vol. 24, pp. 59–74, 2002.

[13] B. Kegl, T. Linder, and K. Zeger, "Learning and design of principal curves," *IEEE Trans. Pattern Anal. Mach. Intell.*, vol. 22, pp. 281–297, 2000.

[14] T. Peng, Y. Wang, T. C. Xu, L. Shi, J. Jiang, and S. Zhu, "Detection of Lung Contour with Closed Principal Curve and Machine Learning," *J. Digit. Imaging*, vol. 31, no. 4, pp. 520–533, 2018.

[15] H. Zhang, W. Pedrycz, D. Miao, and C. Zhong, "A global structure-based algorithm for detecting the principal graph from complex data," *Pattern Recognit.*, vol. 46, no. 6, pp. 1638–1647, 2013.

[16] N. Leema, H. K. Nehemiah, and A. Kannan, "Neural network classifier optimization using Differential Evolution with Global Information and Back Propagation algorithm for clinical datasets," *Appl. Soft Comput.*, vol. 49, pp. 834–844, 2016.

[17] M. Z. Ali, N. H. Awad, P. N. Suganthan, and R. G. Reynolds, "An Adaptive Multipopulation Differential Evolution With Dynamic Population Reduction," *IEEE Trans. Cybern.*, vol. 47, no. 9, pp. 2768–2779, 2017

[18] J. L. J. Laredo, C. Fernandes, J. J. Merelo, and C. Gagné, "Improving genetic algorithms performance via deterministic population shrinkage," in *Proceedings of the 11th Annual conference on Genetic and evolutionary computation - GECCO '09*, Montreal, Canada, 2009, p. 819.

[19] R. Storn, "Differential Evolution – A Simple and Efficient Heuristic for Global Optimization over Continuous Spaces," *J. Glob. Optim.*, p. 19, 1997.

[20] T. Nitta, "An Extension of the Back-Propagation Algorithm to Complex Numbers," *Neural Networks*, vol. 10, no. 8, pp. 1391–1415, 1997.

[21] K. He, G. Gkioxari, P. Dollar, and R. Girshick, "Mask R-CNN," in *Proceedings of the IEEE International Conference on Computer Vision*, Venice, Italy, 2017, pp. 2961–2969.

[22] Z. Zhou, M. M. R. Siddiquee, N. Tajbakhsh, and J. Liang, "UNet++: Redesigning Skip Connections to Exploit Multiscale Features in Image Segmentation," *IEEE Trans. Med. Imaging*, vol. 39, no. 6, pp. 1856–1867, 2020.

[23] T. Peng, Y. Wang, T. C. Xu, and X. Chen, "Segmentation of Lung in Chest Radiographs Using Hull and Closed Polygonal Line Method," *IEEE Access*, vol. 7, pp. 137794–137810, 2019

[24] T. Peng, T. C. Xu, Y. Wang, and F. Li, "Deep Belief Network and Closed Polygonal Line for Lung Segmentation in Chest Radiographs," *Computer J.*, 2020.

Tao Peng received his Ph.D. degree in the Department of Computer Science and Technology at Soochow University in 2019. From 2020 to 2022, he was a postdoctoral researcher in the Department of Health Technology and Informatics at Hong Kong Polytechnic University, and Department of Radiation Oncology at University of Texas Southwestern Medical Center, Dallas, TX, USA, successively. Currently, Dr. Peng is an Associate Professor in School of Future Science and Engineering, Soochow University, Suzhou, China. He has published 34 peer-reviewed journal/conference papers, where the total impact factor (IF) of all the journal publications as the first author is IF > 62. He now serves as a reviewer of more than ten high-quality journal/conference. His main research interests include medical image processing, pattern recognition, machine learning, and their applications.

Jing Zhao, M.D., is a radiologist in the department of ultrasound at the Beijing Tsinghua Changgung Hospital. Her main research interest is medical imaging including diagnosis of prostate and lung diseases and image analysis.

Yanqing Xu is a postdoctoral researcher at McDermott Center for Human Growth and Development, University of Texas Southwestern Medical Center, Dallas, Texas, USA. Her main research interest includes biomedical applications of state-of-the art imaging techniques.

Prof. Jing CAI earned his Ph.D. in Engineering Physics in 2006 and then completed his clinical residency in Medical Physics in 2009 from the University of Virginia, USA. He entered the ranks of academia as Assistant Professor at Duke University in 2009 and was promoted to Associate Professor in 2014. He joined the Hong Kong Polytechnic University in 2017 and is currently a full Professor and the funding Programmer Leader of Medical Physics in the Department of Health Technology and Informatics. He is board-certified in Therapeutic Radiological Physics by the American Board of Radiography (ABR) since 2010. He is the PI/Co-PI for more than 20 external research funds, including 5 NIH, 3 GRF, 3 HMRF, and 1 ITSP grants, with total funding of more than 40M HK Dollars. He has published over 100 papers and 200 conference abstracts and has mentored over 60 trainees as the supervisor. He serves on the editorial boards for several prestigious journals in the fields of medical physics and radiation oncology. He was elected to Fellow of the American Association of Physicists in Medicine (AAPM) in 2018.